arXiv:1703.00628v1 [astro-ph.CO] 2 Mar 2017

J. Astrophys. Astr. (2016) **00**, 000–000

Simulating the z = 3.35 HI 21-cm visibility signal for the Ooty Wide Field Array(OWFA)

Suman Chatterjee[1,2*], Somnath Bharadwaj[1,2†] and Visweshwar Ram Marthi [3‡]

[1] *Department of Physics, IIT Kharagpur, 721302, India*
[2] *Centre for Theoretical Studies, IIT Kharagpur, 721302 , India*
[3] *National Centre for Radio Astrophysics, Tata Institute of Fundamental Research, Post Bag 3, Ganeshkhind, Pune - 411 007, India*

Abstract. The upcoming Ooty Wide Field Array (OWFA) will operate at 326.5 MHz which corresponds to the redshifted 21-cm signal from neutral hydrogen (HI) at z = 3.35. We present two different prescriptions to simulate this signal and calculate the visibilities expected in radio-interferometric observations with OWFA. In the first method we use an input model for the expected 21-cm power spectrum to directly simulate different random realizations of the brightness temperature fluctuations and calculate the visibilities. This method, which models the HI signal entirely as a diffuse radiation, is completely oblivious to the discrete nature of the astrophysical sources which host the HI. While each discrete source subtends an angle that is much smaller than the angular resolution of OWFA, the velocity structure of the HI inside the individual sources is well within reach of OWFA's frequency resolution and this is expected to have an impact on the observed HI signal. The second prescription is based on cosmological N-body simulations. Here we identify each simulation particle with a source that hosts the HI, and we have the freedom to implement any desired line profile for the HI emission from the individual sources. Implementing a simple model for the line profile, we have generated several random realizations of the complex visibilities. Correlations between the visibilities measured at different baselines and channels provides an unique method to quantify the statistical properties of the HI signal. We have used this to quantify the results of our simulations, and

*Email:suman05@phy.iitkgp.ernet.in
†Email:somnath@phy.iitkgp.ernet.in
‡Email:viswesh@ncra.tifr.res.in

explore the relation between the expected visibility correlations and the underlying HI power spectrum.

Key words: cosmology:large scale structure of universe - inter-galactic medium - diffuse radiation

1. Introduction

The redshifted neutral hydrogen (HI) 21-cm radiation is present as a background radiation in all low-frequency radio observations below 1420 MHz. A statistical detection of the random fluctuations in this background radiation present an unique technique for probing the large scale structures in the universe during the post-reionization era ($z \leq 6$) (Bharadwaj, Nath & Sethi 2001; Bharadwaj & Sethi 2001). Observations of high redshift quasars show that the diffuse inter-galactic medium (IGM) is highly ionized at redshifts $z < 6$, and the bulk of the HI in the post-reionization era resides in discrete, dense HI clouds with column densities greater than $2 \times 10^{20}\,\mathrm{atoms\,cm^{-2}}$ (Wolfe et al. 1995; Lanzetta, Wolfe & Turnshek 1995; Storrie-Lombardi, McMahon & Irwin 1996; Péroux et al. 2003). Several measurements of $\Omega_{\mathrm{HI}}(z)$ and $\Omega_{\mathrm{gas}}(z)$ have been carried out both at low and high redshifts. At low redshifts ($z \sim 1$ and lower) we have measurements of $\Omega_{\mathrm{HI}}(z)$ from HI galaxy surveys (Zwaan et al. 2005; Martin et al. 2010; Delhaize et al. 2013) and HI stacking (Lah et al. 2007; Rhee et al. 2013, 2016). Observations of the Damped Ly$-\alpha$ (DLA) systems provide us measurements of $\Omega_{\mathrm{gas}}(z)$ for both low redshifts ($z \sim 1$, Rao, Turnshek & Nestor 2006; Meiring et al. 2011) and high redshifts($2 < z < 6$, Prochaska & Wolfe 2009; Noterdaeme et al. 2012). These observations tell us that the HI content of the universe remains almost constant $\Omega_{\mathrm{gas}}(z) \sim 10^{-3}$ over the entire redshift range $z < 6$ (Lanzetta et al. 1995; Storrie-Lombardi et al. 1996; Rao & Turnshek 2000; Péroux et al. 2003). Unlike traditional galaxy redshift surveys which need to identify individual galaxies in order to map out the large scale structures in the universe, the proposed 21-cm surveys do not need to identify the individual HI sources. The collective redshifted 21-cm radiation from the individual HI clouds appears as a diffuse background radiation and the source clustering is imprinted as the fluctuations in this background radiation.

Future redshifted 21-cm observations are currently perceived to be a very promising probe of the formation and evolution of large-scale structures in the post-reionization era (Bharadwaj & Pandey 2003; Bharadwaj & Ali 2005; Wyithe & Loeb 2008). Such observations hold the potential of measuring the Baryon Acoustic Oscillation (BAO) which is a very sensitive probe of dark energy (Wyithe, Loeb & Geil 2008; Chang et al. 2008; Seo, Dodelson & Marriner 2010; Masui, McDonald & Pen 2010). Further, a measurement

of just the 21-cm power spectrum can also be used to constrain cosmological parameters (Visbal, Loeb & Wyithe 2009; Bharadwaj, Sethi & Saini 2009).

The Giant Meterwave Radio Telescope (GMRT, Swarup et al. 1991) is sensitive to the cosmological HI signal from a range of redshifts in the post-reionization era (Bharadwaj & Pandey 2003, Bharadwaj & Ali 2005) and Ghosh et al. (2011a,b) have carried out preliminary observations towards detecting this signal from $z = 1.32$. The upgraded uGMRT is expected to have a larger bandwidth for which the prospects of a detection are presented in Chatterjee et al. (2017). The Canadian Hydrogen Intensity Mapping Experiment (CHIME, Newburgh et al. 2014 , Bandura et al. 2014) aims to measure the BAO in the redshift range $0.8 - 2.5$. The future Tianlai (Chen 2012, 2015) and SKA1-MID (Bull et al. 2015) also aim to measure the redshifted HI 21-cm signal from the post-reionization era.

The Ooty Radio Telescope (ORT; Swarup et al. 1971) is currently being upgraded (Prasad & Subrahmanya 2011, Subrahmanya et al. 2017b) to a linear radio-interferometric array, the Ooty Wide Field Array (OWFA; Subrahmanya, Manoharan & Chengalur 2017a). The OWFA operates at a nominal frequency of $\nu_o = 326.5\,\mathrm{MHz}$ which corresponds to the redshifted 21-cm signal from a redshift $z = 3.35$. Measuring the redshifted HI 21-cm power spectrum is one of the major science goals of OWFA (Subrahmanya et al. 2017a). Theoretical estimates (Bharadwaj, Sarkar & Ali 2015) predict that it should be possible to measure the amplitude of the 21-cm power spectrum with 150 hrs of observations using OWFA. A more recent study (Sarkar, Bharadwaj & Ali 2017) indicate that it should be possible to measure the 21-cm power spectrum in several different k bins in the range $0.05 - 0.3\,\mathrm{Mpc}^{-1}$ with $1,000$ hrs of observations.

The complex visibilities are the primary quantities measured by any radio-interferometric array like OWFA. It is important and interesting to directly quantify the HI signal in terms of the expected contribution to the measured visibilities. Ali & Bharadwaj (2014) present detailed predictions for the correlations between the visibilities measured at different baselines and frequency channels expected from the statistical HI signal, various astrophysical foregrounds and the system noise. Similar predictions for the HI signal incorporating non-linear effects are also presented in a more recent paper (Gehlot & Bagla 2017). These theoretical estimates predict that the visibilities measured at OWFA will be dominated by astrophysical foregrounds which are expected to be several orders of magnitude larger than the HI signal. Foreground removal (e.g. Ghosh et al. 2011b) is therefore an important issue for detecting the redshifted 21-cm signal. The astrophysical foregrounds are all expected to have a smooth frequency dependence in contrast to the HI signal, and most foreground removal techniques rely on this to distinguish between the foregrounds and the HI signal. However, the chromatic response of the telescope introduces frequency structures in the foregrounds, and it is necessary to model these and account for these in

any foreground removal technique. Here, simulations play a crucial role in modelling the impact of various complicated effects like the telescope's chromatic response, calibration (Marthi & Chengalur 2014) etc. Simulations which incorporate the expected foregrounds, HI signal and also various instrumental and post-processing effects are essential for testing and validating any foreground removal and power spectrum estimation technique.

Marthi (2017) has developed a programmable emulator for OWFA, this provides a platform for simulating the visibilities that will be measured at OWFA. The foreground modelling and predictions are presented in Marthi et al. (2017). In this paper we focus on modelling the HI signal contribution to the visibilities that will be measured at OWFA.

Bagla, Khandai & Datta (2010) have proposed a semi-numerical technique to simulate the redshifted HI signal. This uses N-body simulations to predict the locations and masses of dark matter halos, and relies on a prescription to populate the halos with HI. The same technique has been utilized in subsequent work by Khandai et al.(2011), Guha Sarkar et al.(2012), Villaescusa-Navarro et al. (2014) and Sarkar, Bharadwaj & Anathpindika (2016). It may be noted that this technique requires the N-body simulation to have a rather high spatial resolution $\sim 0.1\,\mathrm{Mpc}$ (comoving) in order to resolve the halos which host the HI. In comparison, an angular extent of 1° and a frequency spread of 1 MHz respectively corresponds to comoving distances of $\sim 113\,\mathrm{Mpc}$ in the transverse direction and $\sim 11.5\,\mathrm{Mpc}$ along the line of sight at $z = 3.35$. Considering the fact that OWFA's field of view (FoV) subtends several degrees on the sky and the bandwidth covers several tens of MHz in frequency, it is computationally prohibitive to implement this technique to directly simulate the signal and calculate the visibilities expected at a Wide Field Array like OWFA.

In this paper we present two different methods to simulate the HI signal and calculate the visibilities expected in observations with OWFA. In the first method we use the results of the semi-numerical simulations (e.g. Bagla, Khandai & Datta 2010) to construct an input model for the expected 21-cm power spectrum. This is used to directly simulate different random realizations of the brightness temperature fluctuations and calculate the visibilities.The HI signal here is assumed to be a Gaussian random field. This method models the HI signal entirely as a diffuse radiation, and is completely oblivious to the discrete nature of the clouds which host the HI.

As noted above, the discrete clouds which host the HI each subtends an angle ($\sim 1''$ or smaller) that is much smaller than the angular resolution (0.1°) of OWFA. The velocity structure ($\sim 100\,\mathrm{km/s}$) of the HI inside the individual clouds, is however well within reach of OWFA's frequency resolution ($\sim 100\,\mathrm{km/s}$ or smaller), and this is expected to have an impact on the observed HI signal. We have also used a second prescription, which is based on earlier work by Bharadwaj & Srikant (2004), uses a cosmological N-body simulation to generate the matter distribution at the desired redshift. Here

we identify each simulation particle with a source that hosts the HI and use this to calculate the expected visibilities. This technique provides us with the freedom to implement any desired line profile for the HI emission from the individual sources. The simulations presented in this paper are preliminary, thermal noise and complicated systematics have not been included here.

A brief outline of the paper follows. In section 2 we present the model 21-cm power spectrum that was used to simulate the HI signal, and Section 3 provides a brief overview of OWFA. The first (direct) simulation technique is presented in Section 4, which also contains the results from this approach. The second (particle based) technique, along with the results, are presented in Section 5. The results from both the simulation techniques are discussed and summarized in Section 6.

We have used the fitting formula of Eisenstein & Hu(1998) for the Λ-CDM transfer function to generate the initial, linear matter power spectrum. The cosmological parameter values used are as given in Ade et al.(2014):$\Omega_m = 0.318$, $\Omega_b\, h^2 = 0.022$, $\Omega_\lambda = 0.682$, $n_s = 0.961$, $\sigma_8 = 0.834$, $h = 0.67$.

2. The 21-cm Power Spectrum

We model the 3D spatial power spectrum $P_T(\mathbf{k})$ of the redshifted 21-cm brightness temperature fluctuations at $z = 3.35$ as

$$P_T\left(\mathbf{k}\right) = \bar{T}^2\ \bar{x}_{\rm HI}^2\ P_{\rm HI}\left(\mathbf{k}\right) \tag{1}$$

where,

$$\bar{T}\left(z\right) = 4.0\, mK\ \left(1+z\right)^2\ \left(\frac{\Omega_b h^2}{0.02}\right)\ \left(\frac{0.7}{h}\right)\ \left(\frac{H_0}{H\left(z\right)}\right) \tag{2}$$

and $P_{\rm HI}\left(\mathbf{k}\right)$ is the power spectrum of the HI density fluctuations, all other symbols have their usual meaning (Bharadwaj & Ali 2005). As mentioned earlier, DLA observations indicate $\Omega_{\rm gas} \simeq 10^{-3}$. This implies that the mass averaged neutral hydrogen fraction has a value $\bar{x}_{\rm HI} = 2.02 \times 10^{-2}$ which we have used in our work. Assuming that the HI gas traces the underlying matter distribution with a linear bias $b_{\rm HI}$, we relate $P_{\rm HI}\left(\mathbf{k}\right)$ to the underlying matter power spectrum $P(\mathbf{k})$ as

$$P_{\rm HI}\left(\mathbf{k}\right) = b_{\rm HI}^2\ \left(1+\beta\mu^2\right)^2\ P(\mathbf{k}) \tag{3}$$

where $\mu = k_\parallel/k$, and $k_\parallel$ is the component of the comoving wave vector $\mathbf{k}$ along the line of sight. The term $\left(1+\beta\mu^2\right)$ arises due to of the effect of HI peculiar velocities (Bharadwaj, Nath & Sethi 2001; Bharadwaj & Ali 2005),

and $\beta = f(\Omega)/b_{\rm HI}$ is the linear redshift distortion parameter, where $f(\Omega)$ is the dimensionless linear growth rate.

We currently do not have any observational constraint on $b_{\rm HI}$ for high redshifts. However, the results from the different semi-numerical simulations, and also an interpolated compilation of $b_{\rm HI}$ values (Padmanabhan, Roy Choudhury & Refregier 2015), indicate that it is reasonably well justified to assume a constant HI bias $b_{\rm HI} = 2$ at wave numbers $k \leq 1\,{\rm Mpc}^{-1}$ at the redshift $z = 3.35$. We have used this value and $\beta = 0.493$ for our entire analysis, this corresponds to $f(\Omega) = 0.986$ (Bharadwaj,Sarkar & Ali 2015).

3. A Brief overview of OWFA

In this paper we consider the so called "Phase-I" of OWFA (e.g. Ali & Bharadwaj 2014, Subrahmanya, Manoharan & Chengalur 2017a) where 24 successive dipoles are combined to form a single antenna which gives rise to a 40 element interferometer. Each antenna element has a rectangular aperture $b \times d$ of dimensions $b = 30\,{\rm m}$ along E-W and $d = 11.5\,{\rm m}$ along N-S respectively. This gives a field-of-view (FoV)of 1.8° (E-W) $\times 4.5^\circ$ (N-S). The 40 antenna elements are equally spaced in a linear array with a separation of 11.5 m along the N-S direction. The telescope is expected to have a frequency bandwidth $B_{bw} = 39$MHz. We assume that the whole bandwidth is divided in $N_c = 312$ frequency channels of $\Delta\nu_c = 125\,{\rm KHz}$ channel width. Note that the values of B_{bw}, N_c and $\Delta\nu_c$ assumed here are only representative values, and the actual values in the final implementation of the telescope may be somewhat different.

The complex visibilities $\mathcal{V}(\mathbf{U},\nu)$ measured by OWFA will be recorded for every independent pair of antennas for every available frequency channel. For any pair of antennas, the baseline $\mathbf{U} = \frac{\mathbf{d}}{\lambda}$ quantifies the antenna separation in units of the observing wavelength. For observation towards the celestial equator, the baselines available at OWFA are

$$\mathbf{U}_n = n\frac{d}{\lambda}\hat{j} \qquad (1 \leq n \leq N_A - 1) \tag{4}$$

where $N_A = 40$ is the total number of antennas for Phase I. There is considerable redundancy in the OWFA baseline distribution in that there are many different antenna pairs which correspond to the same baseline. Any baseline $\mathbf{U}_n$ occurs $M_n = N_A - n$ times in the array. The baseline $\mathbf{U}_n$ corresponding to a fixed antenna separation also changes with the observing wavelength λ.

We have used the flat sky approximation for our calculations throughout this paper. Here $\boldsymbol{\theta}$ is a two dimensional vector in the plane of the sky with the origin at the centre of the FoV. The visibilities $\mathcal{V}(\mathbf{U},\nu)$ are the Fourier transform of the product of the specific intensity distribution on the sky $I(\boldsymbol{\theta},\nu)$ and the telescope's primary beam pattern $A(\boldsymbol{\theta},\nu)$. We calculate the

visibilities using

$$\mathcal{V}(\mathbf{U}_n, \nu_a) = \left(\frac{\partial B}{\partial T}\right) \int d^2\boldsymbol{\theta} A(\boldsymbol{\theta}, \nu_a)\, T(\boldsymbol{\theta}, \nu_a) e^{-2\pi i \mathbf{U}_n \cdot \boldsymbol{\theta}} \tag{5}$$

where $B = 2k_B T/\lambda^2$ is the Planck function in the Raleigh-Jeans limit which is valid at the frequency range of our interest and $T(\boldsymbol{\theta}, \nu)$ is the brightness temperature distribution on the sky.

The primary beam pattern for the rectangular aperture of the antenna elements (Ali & Bharadwaj 2014) can be expressed as

$$A(\boldsymbol{\theta}, \nu) = \mathrm{sinc}^2\left(\frac{\pi b \theta_x}{\lambda}\right) \mathrm{sinc}^2\left(\frac{\pi d \theta_y}{\lambda}\right) \tag{6}$$

where θ_x and θ_y are respectively the x and y components of $\boldsymbol{\theta}$ in a Cartesian coordinate system that is aligned with the plane of the aperture and has the y axis along the N-S direction. We assume this pattern in our simulations, although we note that in practice tapering of the illumination will cause the OWFA element pattern to have lower side lobes and somewhat broader main lobes.

We have decomposed the brightness temperature $T(\boldsymbol{\theta}, \nu)$ as the sum of an uniform average background $\bar{T}_b(\nu)$ and another component $\delta T(\boldsymbol{\theta}, \nu)$ which fluctuates with direction on the sky

$$T(\boldsymbol{\theta}, \nu) = \bar{T}_b(\nu) + \delta T(\boldsymbol{\theta}, \nu)\,. \tag{7}$$

In the flat sky approximation, the visibilities measured at OWFA do not respond to the uniform background $\bar{T}_b(\nu)$ (Ali & Bharadwaj 2014), and it is adequate to only consider the fluctuations $\delta T(\boldsymbol{\theta}, \nu)$ in eq. (5) to calculate the visibilities.

4. Direct Simulation of Brightness Temperature Fluctuations

In this section we present simulations where we use an input model for 3D spatial power spectrum $P_T(\mathbf{k})$ (eq. 1) to directly generate $\delta T(\boldsymbol{\theta}, \nu)$(eq. 7) on the sky and calculate the expected visibilities(eq. 5).

The 326.5 MHz OWFA observations correspond to HI at $z = 3.35$ which is at a comoving distance of $r = 6.84\,\mathrm{Gpc}$. This sets the conversion scale from angular separation to comoving distance in the transverse direction. We further have $r' = \mid dr/d\nu \mid = 11.5\,\mathrm{Mpc\,MHz^{-1}}$ which sets the conversion scale from frequency separation to comoving distance in the radial direction. The OWFA Phase I FoV of $1.8^\circ \times 4.5^\circ$ corresponds to $215\,\mathrm{Mpc} \times 550\,\mathrm{Mpc}$ in the two transverse directions and the bandwidth of $B_{bw} = 39\,\mathrm{MHz}$ corresponds to 449 Mpc in the radial direction.

The simulations were carried out using a N^3 cubic grid of spacing L covering a comoving volume V. We have chosen the grid spacing $L = 1.44\,\mathrm{Mpc}$

so that it exactly matches the channel width $L = r' \times (\Delta\nu_c)$, where the spectral channels are of width $(\Delta\nu_c) = 0.125\,\mathrm{MHz}$. We have considered a $N^3 = [2816]^3$ grid which corresponds to a comoving volume of $[4048\,\mathrm{Mpc}]^3$.The considered volume is kept few times larger to incorporate the side lobe contributions (Figure 2), that comes from the radiation received in the side lobes of the antenna pattern.

We use the input power spectrum $P_T\left(\mathbf{k}\right)$ to generate the Fourier components of the brightness temperature fluctuations

$$\Delta T\left(\mathbf{k}\right) = \sqrt{\frac{V P_T\left(\mathbf{k}\right)}{2}}[a\left(\mathbf{k}\right) + ib\left(\mathbf{k}\right)]\,. \tag{8}$$

on a grid of wave vectors $\mathbf{k}$ corresponding to the simulation volume. Here $a(\mathbf{k})$ and $b(\mathbf{k})$ are two real valued independent Gaussian random variable of unit variance which satisfy

$$\langle a(\mathbf{k})a(\mathbf{k}')\rangle = \langle b(\mathbf{k})b(\mathbf{k}')\rangle = \delta_{\mathbf{k},\mathbf{k}'}\,, \langle a(\mathbf{k})b(\mathbf{k}')\rangle = 0 \;\forall\; \mathbf{k},\mathbf{k}'\,. \tag{9}$$

The Fourier transform of $\Delta T(\mathbf{k})$ yields a single realization of the 21-cm brightness temperature fluctuations $\delta T(\mathbf{x})$ on the simulation grid. These fluctuations are, by construction, a Gaussian random field with the input 21-cm power spectrum. We use different sets of the random variables $a(\mathbf{k})$ and $b(\mathbf{k})$ to generate different statistically independent realizations of $\delta T(\mathbf{x})$. Note that the adopted $P_T(\mathbf{k})$ include the effect of redshift space distortion along the line of sight. Figure 1 shows a comparison of the input model power spectrum with the power spectrum estimated from a single realization of the simulation. We find that the simulated power spectrum is in good agreement with he input model.

The simulation volume is aligned with the z axis along the line of sight. This corresponds to a frequency width of $\sim 9 \times 39\,\mathrm{MHz}$ along the z axis. We have cut the box into 9 equal segments along the line of sight to produce 9 independent realizations each corresponding to a bandwidth of 39 MHz . The grid index, measured from the further boundary and increasing towards to observer along the line of sight was directly converted to channel number $a = 0, 1, 2, ..., N_c - 1$ whereby $\nu_a = 307\,\mathrm{MHz} + aL/r^{'}$. The two transverse directions were restricted to 1553 Mpc and 4048 Mpc along the x and y axes respectively, and these were converted to angles relative to the center $(\theta_x,$ $\theta_y) = (x/r,\ y/r)$. The extent along the x and y axes were chosen so as to contain approximately the first three nulls of the beam pattern $A(\boldsymbol{\theta}, \nu_a)$ (bottom panel of Figure 2) along each direction. The cut out region of the simulation box procedure provides us with $\delta T(\boldsymbol{\theta}, \nu_a)$ the brightness temperature fluctuation on the sky (upper panel of Figure 2) at different frequency channels ν_a.

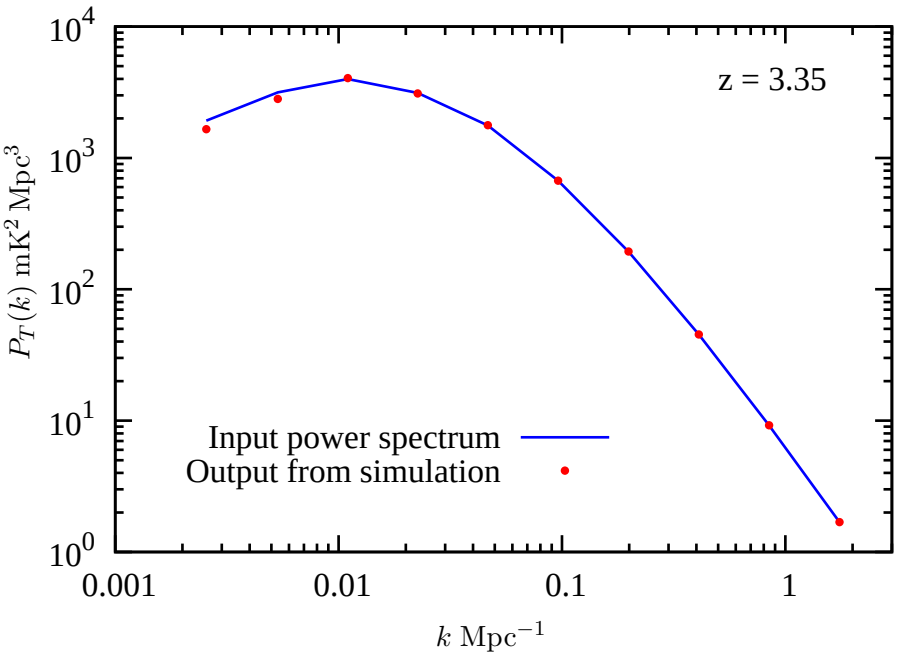

Figure 1. The solid blue curve shows the input model 21-cm brightness temperature power spectrum $P_T(k)$, and the points show $P_T(k)$ calculated from one realization of the simulation. Both have been averaged over μ to remove the μ dependence.

We calculate the visibilities using a discretized version of eq. (5) whereby

$$\mathcal{V}(\mathbf{U}_n, \nu_a) = \left(\frac{\partial B}{\partial T}\right)(\Delta\theta)^2 \sum_g A(\boldsymbol{\theta}_g, \nu_a)\delta T(\boldsymbol{\theta}_g, \nu_a) e^{-2\pi i U_n \theta_{yg}} \tag{10}$$

where $\Delta\theta$ is the angular resolution of the simulation grid, the sum is over all the grid points (labelled using g) corresponding to the fixed frequency channel ν_a, and θ_{yg} is the y component of the vector $\boldsymbol{\theta}_g$ corresponding to the grid point g.

The baseline and frequency channel configuration of OWFA Phase I probes the $k_\perp$ range $k_{\perp_{min}} = 1.1\times10^{-2}\,\mathrm{Mpc}^{-1}$ to $k_{\perp_{max}} = 4.8\times10^{-1}\,\mathrm{Mpc}^{-1}$, and the $k_\parallel$ range $k_{\parallel_{min}} = 1.4\times10^{-2}\,\mathrm{Mpc}^{-1}$ to $k_{\parallel_{max}} = 2.73\,\mathrm{Mpc}^{-1}$ (Bharadwaj et al. 2015). For our simulations we have the corresponding values $k_{\perp_{min}} = 1.4\times10^{-3}\,\mathrm{Mpc}^{-1}$, $k_{\perp_{max}} = 4.37\,\mathrm{Mpc}^{-1}$, $k_{\parallel_{min}} = 1.4\times10^{-2}\,\mathrm{Mpc}^{-1}$ and $k_{\parallel_{max}} = 2.73\,\mathrm{Mpc}^{-1}$. As can be seen our simulations adequately cover the entire k range that will be probed by OWFA Phase I.

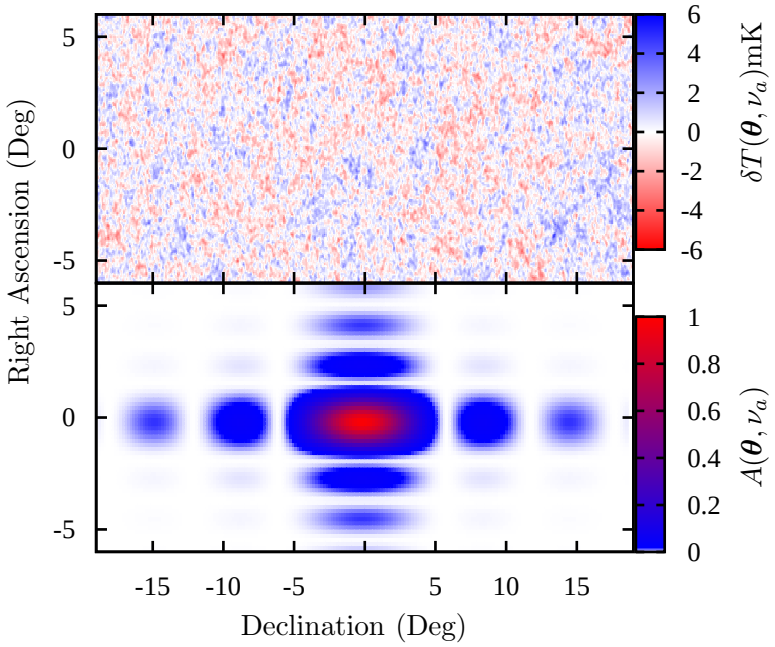

Figure 2. The upper panel shows a single realization of the simulated redshifted 21-cm brightness temperature fluctuations $\delta T(\boldsymbol{\theta}, \nu_a)$ as a function of $\boldsymbol{\theta}$ for a fixed ν_a corresponding to the central frequency channel. Note that the angular extent shown here corresponds to the region which was actually cut out from the entire simulation volume and used to calculate the OWFA visibilities. The lower panel shows a similar plot of the beam pattern $A(\boldsymbol{\theta}, \nu_a)$.

4.1 *Validating the simulation*

The redshifted 21-cm brightness temperature fluctuations are, by construction, a Gaussian random field. The visibilities obtained from the simulations also are random, and each realization of the simulation will yield a different set of values for the visibilities. It is necessary to consider the statistical properties of the simulated visibilities in order to validate the simulations. In this paper we consider the correlations between the visibilities at two different baselines $\mathbf{U}_n$ and $\mathbf{U}_m$ and two different frequencies ν_a and ν_b

$$V_2(\mathbf{U}_n, \mathbf{U}_m, \nu_a, \nu_b) = \langle \mathcal{V}(\mathbf{U}_n, \nu_a) \mathcal{V}^*(\mathbf{U}_m, \nu_b) \rangle \, . \tag{11}$$

The angular brackets $\langle ... \rangle$ here denote an ensemble average over different realizations of the simulation. The HI contribution to the two-visibility correlation is directly related to the power spectrum $P_T(\mathbf{k})$ (Bharadwaj & Sethi 2001; Bharadwaj & Ali 2005). For OWFA we have (Ali & Bharadwaj

2014),

$$V_2(\mathbf{U}_n, \mathbf{U}_m, \nu, \nu + \Delta\nu) = \left(\frac{\partial B}{\partial T}\right)^2 \int d^2U' \tilde{a}(\mathbf{U}_n - \mathbf{U}', \nu)$$
$$\times \quad \tilde{a}^*(\mathbf{U}_m - \mathbf{U}', \nu + \Delta\nu) \left[\frac{1}{\pi r^2} \int_0^\infty dk_\parallel \cos(k_\parallel r' \Delta\nu) P_T(\mathbf{k})\right] \qquad (12)$$

where $\tilde{a}(\mathbf{U}, \nu)$ is the Fourier transform of the beam pattern $A(\boldsymbol{\theta}, \nu)$ and $\mathbf{k}$ refers to a comoving wave vector with radial and transverse components $k_\parallel$ and $(2\pi/r)\,\mathbf{U}'$ respectively. In evaluating this expression it has been assumed that for all the terms in the *r.h.s.* the variation with ν is much slower in comparison with the variation with $\Delta\nu$. As a consequence we have held the values of r,$r^{'}$, $(\partial B/\partial T)$ and $\mathbf{U}_n$ fixed at that corresponding to the central frequency.

Earlier work (Ali & Bharadwaj 2014) has shown that for OWFA the visibility correlation $V_2(\mathbf{U}_n, \mathbf{U}_m, \nu_a, \nu_b)$ has non-zero values only for the situation when the two baselines are the same $(m = n)$ or if they are adjacent $(|m - n| = 1)$, the correlation is zero in all other situations. Further, the correlation is approximately four times smaller if we consider adjacent baselines instead of the same baseline (Bharadwaj et al. 2015). In this paper we have restricted the analysis to the situation where $n = m$ and we have considered

$$V_2(\mathbf{U}_n, \Delta\nu) \equiv V_2(\mathbf{U}_n, \mathbf{U}_n, \nu_a, \nu_b) \qquad (13)$$

with $\Delta\nu =\mid \nu_a - \nu_b \mid$ to validate the simulations.

We have used 180 independent realizations of the simulated visibilities to evaluate the two-visibility correlation $V_2(\mathbf{U}_n, \Delta\nu)$ (eq. 11). The results thus obtained were compared with the linear theory predictions (eq. 12) in order to validate the simulations.

4.2 *Results*

We first consider the visibility correlation $V_2(\mathbf{U}_n, 0)$ which corresponds to the situation where $\Delta\nu = 0$. In this case we have $\cos(k_\parallel r' \Delta\nu) = 1$ in eq. (12) for which the visibility correlation $V_2(\mathbf{U}_n, \Delta\nu)$ is maximum.

Figure 3 shows a comparison between the linear theory predictions (line) and the simulations (points). The 1σ error bars on simulated data points are estimated from the 180 independent realizations of the simulated visibilities. We see that the simulations are in very good agreement with the linear theory predictions.

We next consider how the visibility correlation $V_2(\mathbf{U}_n, \Delta\nu)$ varies with respect to $\Delta\nu$. It is convenient to use the frequency decorrelation function $\kappa_{U_n}(\Delta\nu)$ (Datta, Roy Choudhury & Bharadwaj 2007) which is defined as

$$\kappa_{U_n}(\Delta\nu) = \frac{V_2(\mathbf{U}_n, \Delta\nu)}{V_2(\mathbf{U}_n, 0)}\,. \qquad (14)$$

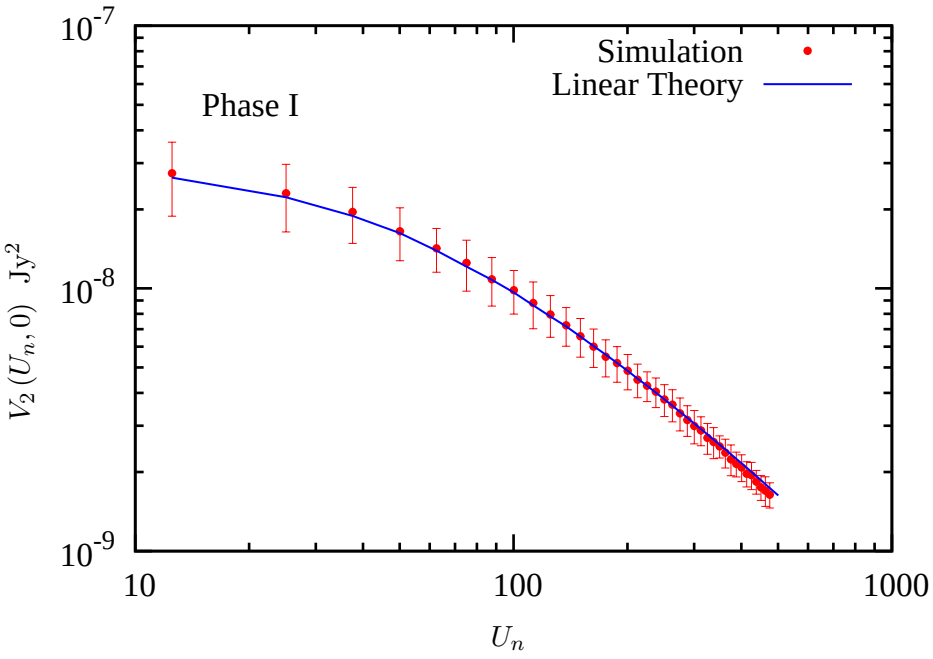

Figure 3. The solid curves shows the linear theory predictions (eq. 12) for the HI signal $V_2\,(U, \Delta\nu)$ for $\Delta\nu = 0$, and the points show the results from the simulations (eq. 11). The 1σ error bars on the simulated data points are estimated from 180 independent realizations of the simulated visibilities.

This quantifies how rapidly the HI signal decorrelates as we increase the frequency separation $\Delta\nu$. The correlation is maximum for $\Delta\nu = 0$ where $\kappa_{U_n}\,(\Delta\nu = 0) = 1$, and the linear theory analytic calculations (Ali & Bharadwaj 2014) predict the correlation to fall as $\Delta\nu$ is increased. Figure 4 shows the variation of the decorrelation function as a function of $\Delta\nu$ for different values of U_n. We observe that the simulations (dashed lines) are in good agreement with the linear theory predictions (solid lines) for all values of U_n. The HI signal decorrelates slowly with increasing $\Delta\nu$ at the short baseline (e.g. $U_n = 12.5$ for $n = 1$) in comparison to the long baselines (e.g. $U_n = 250$ for $n = 20$) where the HI signal decorrelates relatively rapidly. We see that for $n = 1$ we have $\kappa_{U_n}\,(\Delta\nu) = 0.5$ at $\Delta\nu \approx 1\,\mathrm{MHz}$ beyond which the value of $\kappa_{U_n}\,(\Delta\nu)$ falls further. In comparison, for $n = 20$ we have $\kappa_{U_n}\,(\Delta\nu) = 0.5$ at a smaller frequency separation of $\Delta\nu \approx 0.4\,\mathrm{MHz}$.

In summary here, we note that our results show that the simulations faithfully reproduce both the U_n and the $\Delta\nu$ dependence of the visibility correlation $V_2(\mathbf{U}_n, \Delta\nu)$ expected from the linear theory predictions (eq. 12) thereby validating the simulations.

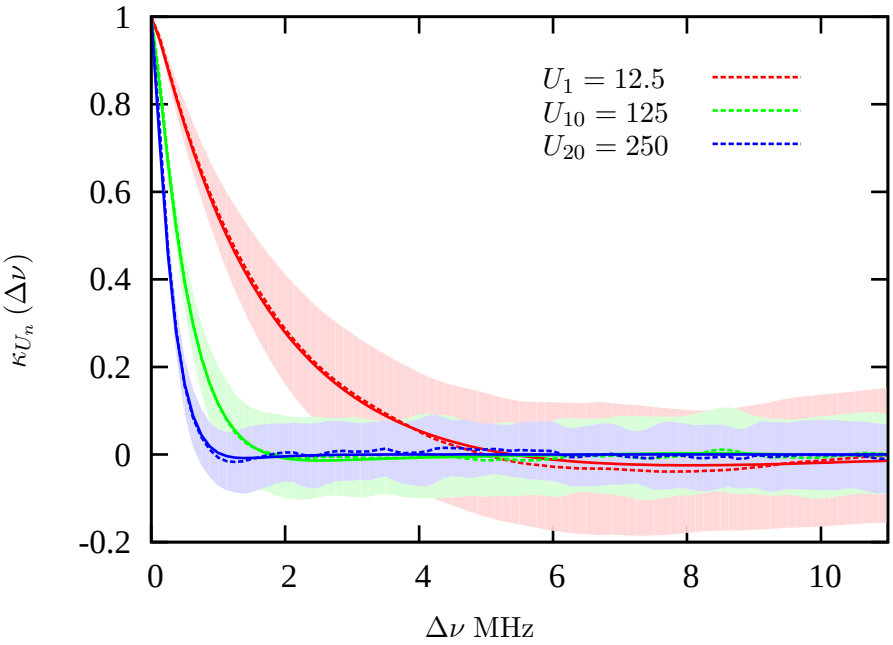

Figure 4. This shows the frequency decorrelation functions $\kappa_{U_n}(\Delta\nu)$ as a function of $\Delta\nu$ at three different U_n values. Solid lines show the linear theory predictions and dashed lines are the results obtained from the simulations.The shaded regions show the $1\,\sigma$ variation measured from 180 realizations of the simulated visibilities. We see that the signal decorrelates more rapidly at the longer baselines as compared to the shorter ones.

5. Particle Based Simulation

The simulations presented in the previous section treat the HI signal entirely as a diffuse radiation field and are completely oblivious to the discrete nature of the astrophysical sources which host the HI. While each discrete source subtends an angle that is much smaller than the angular resolution of OWFA, the velocity structure of the HI inside the individual sources is well within reach of OWFA's frequency resolution and this is expected to have an impact on the observed HI signal.In this section we outline a particle based simulation which allows the flexibility of introducing any desired line profile for the radiation from the individual sources. The simulation technique here follows an earlier work (Bharadwaj & Srikant 2004).

The simulation uses a cosmological Particle Mesh (PM) N-body code to generate the dark matter particle distribution at $z = 3.35$. The simulations were done using a $N^3 = [2048]^3$ grid which corresponds to a comoving volume of $[2944\,\mathrm{Mpc}]^3$ with $[1024]^3$ particles in it. We have chosen the grid spacing $L = 1.4375\,\mathrm{Mpc}$ so that it exactly matches the frequency channel width

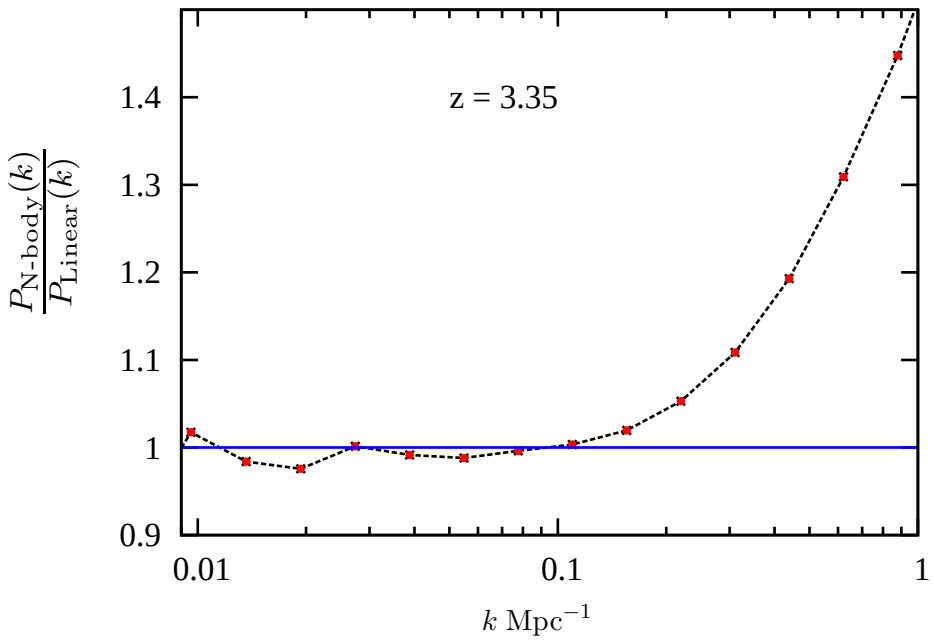

Figure 5. This shows the ratio of the power spectrum of density fluctuations from N-body simulations and the $z = 3.35$ linear theory predictions. The power spectra shown here do not incorporate redshift space distortions.

$L = r^{'} \times (\Delta\nu_c)$. We also incorporate the redshift space distortion effect from the velocity information of the dark matter particles. Figure 5 shows the ratio of the power spectrum of the density fluctuations in the dark matter distribution from N-body simulations and the power spectrum obtained from linear theory at $z = 3.35$. We find that the power spectrum obtained from the N-body simulation starts showing deviations from the linear power spectrum at Fourier modes $k \geq 0.2\text{Mpc}^{-1}$ and the deviation increases as we move on to higher k modes. These deviations are a consequence of the non-linear evolution of the density fluctuations at small scales. This is an additional feature where the present technique improves upon the method presented in the previous section. We remind the reader that the previous method was entirely based on the predictions of linear theory.

We have cut the simulation box into 6 equal segments along the line of sight to produce 6 independent realizations each corresponding to 39 MHz along the line of sight. The simulation boxes were further cut to have dimensions 1130 Mpc and 2944 Mpc respectively along the x and y axes, and the particle distribution in the resulting boxes was used to calculate the HI signal. We assume that the hydrogen has a mean neutral fraction $\bar{x}_{HI} = 2.02 \times 10^{-2}$ and the total HI content is equally distributed amongst

all the N-body particle, whereby distribution follows the underlying particle density $n(\mathbf{x})$. Incorporating this, we model the redshifted 21-cm brightness temperature distribution in the simulation box as

$$T(\mathbf{x}) = \bar{T}\,\bar{x}_{\rm HI}\,b_{\rm HI}\,\frac{n(\mathbf{x})}{\bar{n}} \tag{15}$$

where the factor $b_{HI} = 2.0$ introduces the linear bias, $\bar{n}$ is the mean particle density, and

$$n(\mathbf{x}) = \sum_{i=1}^{N} \delta^3(\mathbf{x} - \mathbf{x}_i) \tag{16}$$

where $\mathbf{x}_i$ refers to the positions of the individual particles in redshift space. It is important to note that the impact of the discrete nature of the HI sources depends on $\bar{n}$ the number density of HI clouds. The actual number density of the HI cloud around $z = 3.35$ is not known, and in this work we have arbitrarily set $\bar{n} = 0.04\,{\rm Mpc}^{-3}$ which corresponds to the particle number density in the simulation.

In the last section we described how we map the brightness temperature distribution $T(\mathbf{x})$ to a brightness temperature distribution $T(\boldsymbol{\theta}, \nu)$ in angle and frequency in order to calculate the visibilities (eq. 5). The position of each simulation particle $\mathbf{x}_i$ also undergoes a similar mapping. As mentioned earlier, the two transverse dimensions are mapped to angles $(\theta_{ix}, \theta_{iy}) = (x_i/r,$ $y_i/r)$ and the radial direction is mapped to frequency $(\nu_i = 307\,{\rm MHz} + z_i/r^{'})$ where all the positions and angles are all with reference to the box center. Here, the HI radiation from a particular source at a radial distance of z_i will be received at a single frequency ν_i which is determined by the cosmology, and the particular source will not contribute to any of the other frequencies. In reality, the HI emission emanating from any astrophysical source will have a spread in frequencies due to a variety of reasons including the thermal line broadening and the bulk motions of the HI gas inside the source. We include this in the simulation by introducing a line profile $\phi_i(\nu - \nu_i)$ associated with each source. The line profile determines the frequency spread of the redshifted HI 21-cm emission from a particular source, and it is normalized as

$$\int \phi_i(\nu) d\nu = 1 \tag{17}$$

While the line profile may, in principle, differ from source to source we have here assumed the same line profile for all the sources in order to keep the analysis simple. It may further be noted that the line profile here has been defined with respect to the observed frequency in the rest frame of the telescope. Using eq (15) in eq. (5) and incorporating the line profile, we obtain

a relation which allows us to calculate the OWFA visibilities corresponding to the simulated particle distribution

$$\mathcal{V}(U_n,\nu_a) = \left(\frac{\partial B}{\partial T}\right)\frac{\bar{T}}{\bar{n}r^2r'}\sum_i A(\boldsymbol{\theta}_i,\nu_i)\phi(\nu_a-\nu_i)e^{2\pi i U_n\theta_{yi}}\,. \tag{18}$$

While we have the freedom of implementing any desired line profile for the HI sources, for the purpose of this paper we have chosen a very simple line profile

$$\begin{aligned}\phi(\nu-\nu_i) &= \frac{1}{F\,\Delta\nu_c} \qquad \text{for } \mid \nu-\nu_i \mid \leq \frac{F}{2}\times\Delta\nu_c \\ &= 0 \qquad\qquad\qquad\quad \text{otherwise}\,.\end{aligned} \tag{19}$$

Here we have considered three values of $F = 1, 2, 3$. For $F = 1$ every source here is assigned a flat line profile of width 0.125 MHz, which is also the frequency resolution assumed for OWFA, this corresponds to a velocity spread of $114\,\mathrm{kms}^{-1}$ at the rest frame of the source, which is a reasonable value for the HI velocities inside the individual sources expected at this redshift. For $F = 2$ and 3 the assigned flat line profiles are of broader width 0.25 MHz and 0.375 MHz, which respectively correspond to twice and thrice the frequency resolution of OWFA.

5.1 *Results*

Figure 6 shows the visibility correlation $V_2\,(U_n, 0)$ determined from the simulations. We have run 180 independent realizations of the simulation for which the mean and the standard deviation are respectively shown with points and the corresponding error bars. We find that for all values of F the value of $V_2\,(U_n, 0)$ obtained from the simulations is approximately twice the linear prediction for the shortest baseline U_n with $n = 1$. For $F = 1$ the values obtained from the simulations are considerably larger than the linear theory prediction (solid line) for all values of U_n. The simulated values are roughly a factor of 1.3 times larger than the linear prediction in the baseline range $20 \leq U_n \leq 100$ which corresponds to $2 \leq n \leq 8$, the deviation between the simulations and the linear theory predictions is found to increase at longer baselines $U_n > 100$. Barring the shortest baseline, the values of $V_2\,(U_n, 0)$ progressively decrease as F is increased to 2 and 3. For $F = 2$ the results are still in excess of the linear predictions. For $F = 3$ the results match with the linear theory predictions for $U_n < 100$ whereas the results are below the linear theory predictions for larger baselines. The deviations from linear theory seen for $F = 1, 2$ and 3 can be attributed to a combination of the effect of the finite line width (eq. 19) and the non-linear evolution of the particle distribution in the N-body simulations (Figure 5). However, we expect the non-linear evolution to be more significant at the

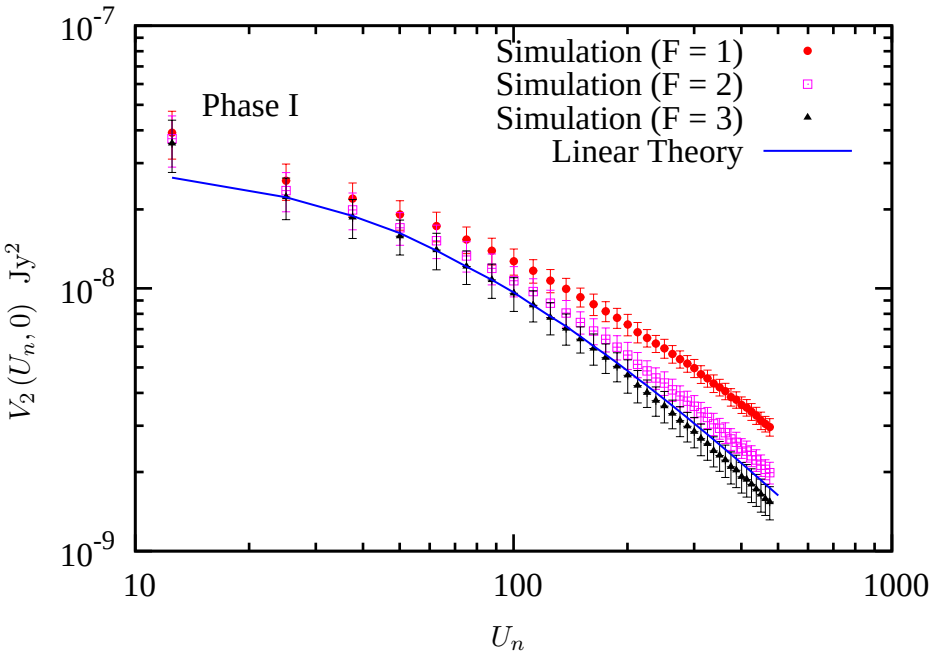

Figure 6. The solid curve shows the linear theory predictions, and the points in different styles (see legend) show the results from the simulations. The $1\,\sigma$ error bars are estimated from 180 realizations of the simulations.

longer baselines, and it is difficult to use these two effects to explain why the shortest baseline shows a larger deviation compared to the other adjacent longer baselines for all values of F.

The earlier work (Ali & Bharadwaj 2014) has shown that the OWFA visibilities only respond to the brightness temperature fluctuations $\delta T(\boldsymbol{\theta}, \nu)$, and are insensitive to the mean component $\bar{T}_b(\nu)$. This however had assumed the flat sky approximation, and the sky was assumed to have an infinite extent. This however does not hold for the simulations which also assume the flat sky approximation but have a finite sky extent. The sinc^2 primary beam pattern (eq. 6) is now truncated after a finite extent and as a consequence the visibilities all pick up a contribution from $\bar{T}_b(\nu)$. This contribution could be relatively large for the short baselines, however it is expected to die down at the longer baselines. We can explain the large deviation at the shortest baseline by attributing it to the mean component $\bar{T}_b(\nu)$ that is picked up due to the finite sky coverage. We note that this problem does not arise in the previous section where the mean component is not included in the simulations.

In order to verify our understanding of the origin of the large deviation at the shortest baseline, we have considered a situation where the brightness

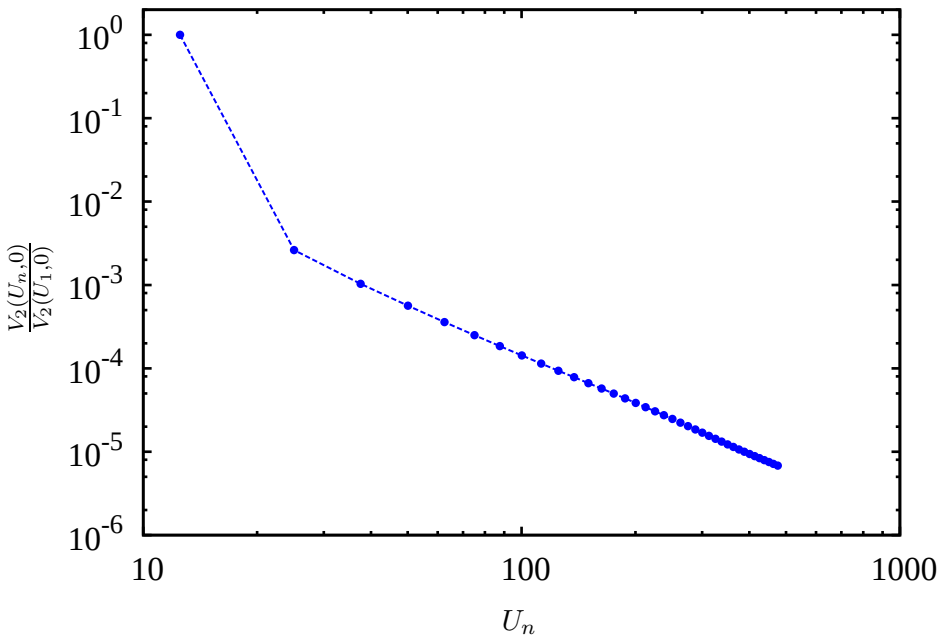

Figure 7. Considering a simulation where the brightness temperature distribution has only a mean contribution $\bar{T}_b(\nu)$, this shows the ratio $V_2(U_n, 0)/V_2(U_1, 0)$ as a function of U_n.

temperature distribution (eq. 7) has only a contribution from $\bar{T}_b(\nu)$ and the fluctuations $\delta T(\boldsymbol{\theta}, \nu)$ have been set to zero. These simulations were run for $F = 1$ only. Considering the ratio $V_2(U_n, 0)/V_2(U_1, 0)$ (Figure 7) we find that this falls by approximately three orders of magnitude as we go from $n = 1$ to $n = 2$. The ratio falls even further if we consider longer baselines $n > 2$. This supports our interpretation that in our simulations the shortest baseline picks up a significant contribution from the mean brightness temperature, however this contamination is not significant at the longer baselines.

Figure 8 shows the variation of $\kappa_{U_n}(\Delta\nu)$ with $\Delta\nu$ for three different baselines. Notice that $\kappa_{U_n}(\Delta\nu)$ obtained from the simulations at the shortest baseline saturates at a relatively large value (~ 0.25) at frequency separations $\Delta\nu > 4\,\mathrm{MHz}$ in contrast to the linear predictions which are close to zero in this range. A similar discrepancy is not seen at the longer baselines where both the simulations and the linear prediction are close to zero for large $\Delta\nu$. This discrepancy at the shortest baseline also can be explained by the fact that the shortest baseline picks up a relatively large contribution from $\bar{T}_b(\nu)$ due to the limited angular extent of the simulations. This problem does not seem to be significant at the longer baselines, and we have

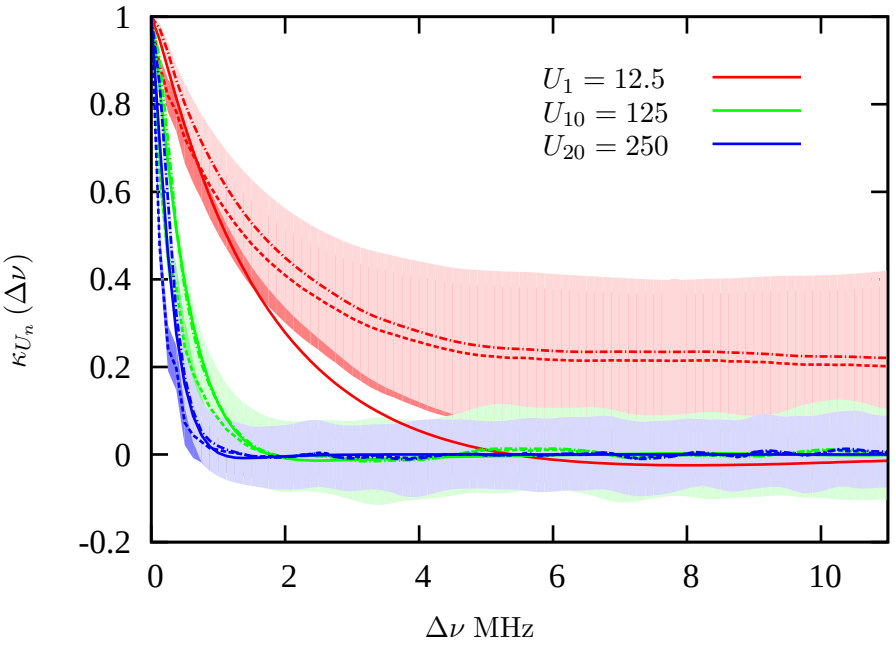

Figure 8. This shows the linear theory (solid line) and simulated (dashed line for $F = 1$, dot-dashed line for $F = 3$) $\kappa_{U_n}(\Delta\nu)$ as a function of $\Delta\nu$ at three different U_n values.

dropped the shortest baseline from the subsequent discussion of this section.

For these simulations we find that it is more convenient to directly study $V_2(U_n, \Delta\nu)$ instead of considering $\kappa_{U_n}(\Delta\nu)$ to analyze how the visibility correlation behaves as a function of $\Delta\nu$. Figures 9 and 10 show $V_2(U_n, \Delta\nu)$ as a function of $\Delta\nu$ for the two values $U_n = 150$ and 450 respectively. We have already seen that for $F = 1$ the values of $V_2(U_n, 0)$ from the simulations are ~ 1.3 times larger than the linear prediction in the range $20 \leq U_n \leq 100$ (Figure 6), and this discrepancy increases at longer baselines $U_n > 100$. Here we find that for $F = 1$, $V_2(U_n, 0)$ from the simulations are ~ 1.5 times larger than the linear prediction at $U_n = 150$ (Figures 9). The discrepancy in $V_2(U_n, 0)$ is reduced for $F = 2$ and the results are roughly consistent with linear theory for $F = 3$. We further see that the discrepancies are restricted to $\Delta\nu = 0$ only for all values of F. The simulations are consistent with the linear predictions for larger values of $\Delta\nu$, except possibly for a slight excess seen at $\Delta\nu = 0.125$MHz for $F = 2$. The discrepancy at $\Delta\nu = 0$ arises from the line profile $\phi(\nu)$. The HI emission from any individual source in the simulation will be spread across a finite frequency width introducing an excess correlation within the line width (Bharadwaj & Srikant 2004). For

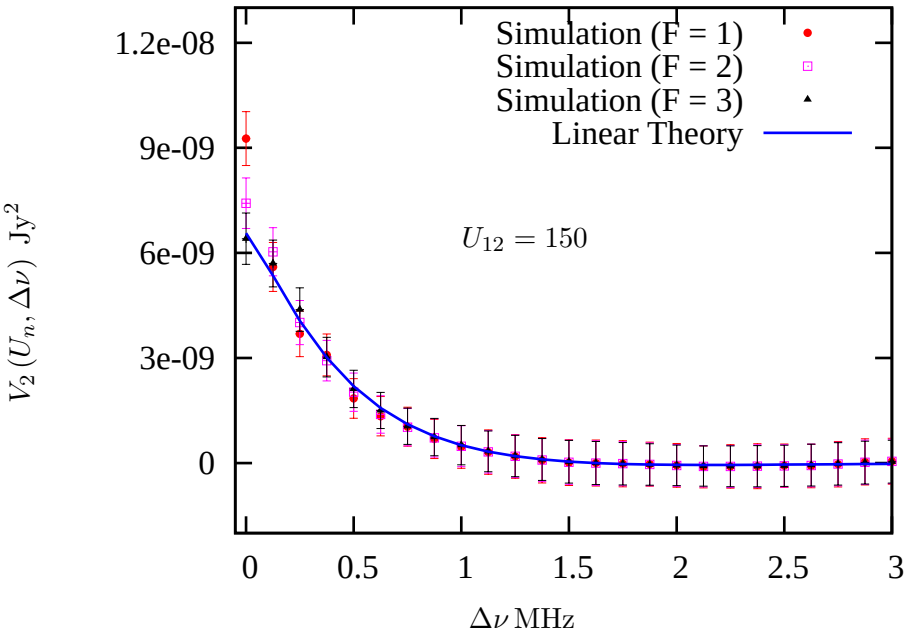

Figure 9. The solid curve shows the linear theory predictions for the visibility correlation $V_2\,(U_n, \Delta\nu)$, and the points in different styles (see legend) show the results from the simulations as a function of $\Delta\nu$ for $U_n = 150$ with $n = 12$.

$F = 1$ the line width is the same as the channel width $\Delta\nu_c$ which is why the discrepancy is only limited to $\Delta\nu = 0$ and does not extend to larger frequency separations for $F = 1$. For $F = 2$ the line width is doubled and its height is halved. This explains why the deviation from linear theory in $V_2(U_n, 0)$ drops relative to $F = 1$. This is also possibly responsible for the small excess that we see at $\Delta\nu = 0.25\,\mathrm{MHz}$ for $F = 2$. For $F = 3$ the line width is thrice that for $F = 1$ whereas its height is three times smaller. There is no noticeable excess correlation seen for $F = 3$ because of the reduced line height, and the results are consistent with linear theory for all values of $\Delta\nu$.

We next consider a larger baseline $U_n = 450$ for which $V_2(U_n, \Delta\nu)$ is shown in Figure 10. For $F = 1$ we find that the value obtained from the simulations is ~ 1.5 times larger than the linear prediction for $\Delta\nu = 0$ and the simulations are consistent with the linear predictions for all larger values of $\Delta\nu$. For $F = 2$ the discrepancy from the linear predictions reduces in magnitude but it now extends to $\Delta = \nu = 0$ and $0.125\,\mathrm{MHz}$. For $F = 3$ the result from the simulation falls below the linear prediction at $\Delta\nu = 0$ while we have an excess at $\Delta\nu 0.125\,\mathrm{MHz}$ and $0.25\,\mathrm{MHz}$. In summary we find that the magnitude and frequency extent of the deviations from the

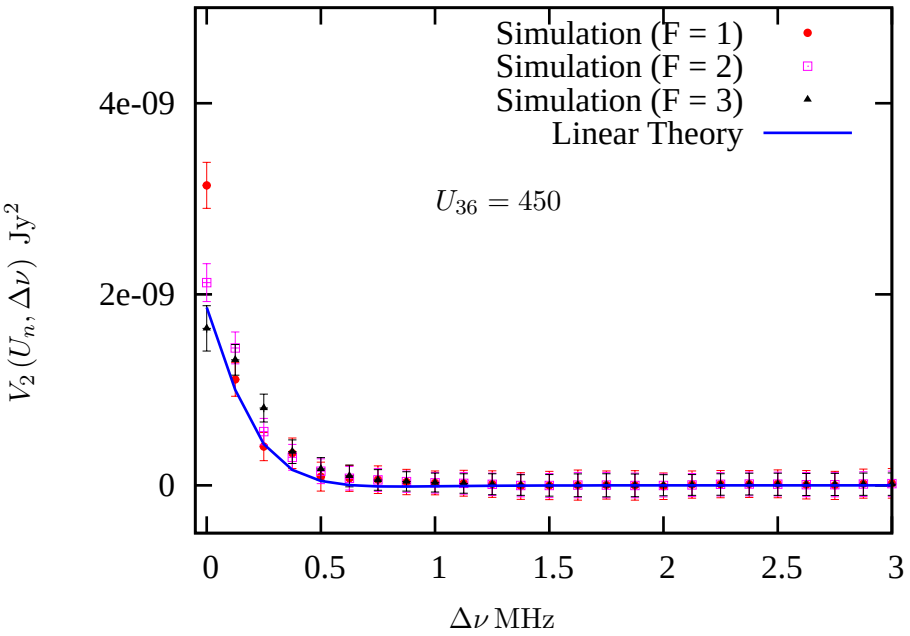

Figure 10. The solid curve shows the linear theory predictions for the visibility correlation $V_2\,(U_n, \Delta\nu)$, and the points in different styles (see legend) show the results from the simulations as a function of $\Delta\nu$ for $U_n = 450$ with $n = 36$.

linear predictions is strongly correlated with the value of F which decides the frequency width and height of the HI emission line from the individual sources. This leads to a picture where the deviations from linear theory seen in Figures 6, 8,9 and 10 can be largely attributed to the effect of the line profile of the individual HI sources. In the present analysis we are unable to identify any noticeable signature of he non-linear evolution of the underlying dark matter distribution. Finally we note that the good agreement between the simulations and the linear predictions found at the long baselines for large frequency separations confirms the fact that the longer baselines do not pick up a significant contribution from $\bar{T}_b(\nu)$.

6. Discussion

In this paper we present two different methods for simulating the redshifted HI 21-cm visibility signal expected in observations with Phase I of OWFA. The first method directly generates random realizations of the brightness temperature fluctuations $\delta T(\boldsymbol{\theta}, \nu)$ corresponding to the input model power spectrum $P_T(\mathbf{k})$ at $z = 3.35$ (eq. 1). These simulations treat the HI signal entirely as a diffuse radiation and ignores the fact that the HI actually resides

in discrete clouds. Further, it also assumes that the redshifted 21-cm radiation is a Gaussian random field whose properties are completely described by the power spectrum $P_T(\mathbf{k})$ calculated using linear perturbation theory. The second method uses a cosmological N-body simulation to generate a $z = 3.35$ particle distribution. We identify these particles as the discrete sources that host the HI. This method allows us the freedom to assign any desired line profile to the HI emission from the individual sources. It also captures the non-linear evolution of the density field. For the present work we have used a simple line profile where each source is assigned an uniform line width. The simulations were done for three different line widths $\Delta\nu = 0.125\,\mathrm{MHz}, 0.25\,\mathrm{MHz}$ and $0.375\,\mathrm{MHz}$ which respectively correspond to $F = 1, 2$ and 3 in our model for the line profile.

The simulated visibilities, in both cases, are a random signal. We have considered the two-visibility correlation $V_2(U_n, \Delta\nu)$ to analyze the results of the simulations and compare them with the predictions of linear theory. As expected, we find that the first method faithfully reproduces the predictions of linear theory. For the second method, we find that the visibilities at the shortest baseline pick up a relatively large contribution from $\bar{T}_b(\nu)$ possibly due to the limited sky coverage of the simulations. The visibilities at the longer baselines are not significantly contaminated by a contribution from $\bar{T}_b(\nu)$. We consider two long baselines, $U_n = 150$ and 450 respectively in order to analyze the results of the second method. We find that the results from the simulations show discrepancies from the linear theory predictions. These discrepancies are restricted to $\Delta\nu$ values which are comparable to or smaller than the frequency width of the line profile, and the simulations are consistent with linear theory at larger $\Delta\nu$. The magnitude of the discrepancy depends on the width of the line profile, and for $F = 1$ we find an excess over the linear predictions at $\Delta\nu = 0$. The magnitude of this excess comes down when F is changed from 1 to 2. We interpret this as arising from the fact that height of the line profile is halved when F is changed from 1 to 2. We find that the simulations fall below the linear theory prediction at $\Delta\nu = 0$ for $F = 3$. In this case the increased line width possibly smears out some of the correlation, and the line height is also further reduced .

In conclusion we note that simulated data generated using the methods presented in this paper will play an important role in validating the OWFA data analysis pipeline. Simulated data will also play an important role in correctly interpreting the observed HI signal once a detection is made. In this work we find that it is important to take into account the discrete nature of the HI coulds. The line profile of the individual HI clouds play an imprtant role in shaping the statistical properties of the redshifted 21-cm signal at small frequency separations which are comparable to the line width of the emission from the individual clouds. We note that similar results have been reported in an earlier paper (Bharadwaj & Srikant 2004). For the present work we have used a rather simplistic line profile, we plan to incorporate

more realistic models for the HI line profile in future work. Further, the impact of the discrete nature of the HI sources depends on $\bar{n}$ the number density of HI clouds which has been set arbitrarily to $\bar{n} = 0.04\,\mathrm{Mpc}^{-3}$ which corresponds to the particle number density in the simulation. We plan to consider more realistic HI mass distribution schemes in future work.

The current work reveals that the flat-sky paradigm adopted here fails to correctly model the visibilities at the shortest baseline, and it is necessary to implement the spherical sky in order to correctly handle this. This is also expected to be important for OWFA Phase II which will have a much larger field of view. We plan to also address this in subsequent work.

Acknowledgement

The authors would like to thank Jayaram Chengalur for the useful suggestions and discussions. SC acknowledges the University Grant Commission, India for providing financial support through Senior Research Fellowship. SC would also like to thank Anjan Kumar Sarkar and Debanjan Sarkar for their help and useful discussions.

References

Ade, P. A. R., Aghanim, N. et al. 2014, A&A, 571, A16.
Ali S. S., Bharadwaj S.,2014, JApA, 35, 157
Bagla J. S., Khandai N., Datta K. K., 2010, MNRAS, 931
Bandura K., Addison G.E., Amiri M., et al. 2014, Proc. SPIE 9145, Ground-based and Airborne Telescopes V, 914522
Bharadwaj S., Nath B., Sethi S. K., 2001, JApA, 22, 21
Bharadwaj S., Sethi S. K., 2001, JApA, 22, 293
Bharadwaj S., Ali S. S., 2005, MNRAS, 356, 1519
Bharadwaj S., Sethi S., Saini T. D., 2009, Phys Rev. D, 79, 083538
Bharadwaj S., Sarkar A. K., Ali, S. S., 2015 JApA 36(3), 385-398
Bharadwaj S., Pandey S. K., 2003, JApA, 24, 23
Bharadwaj S., Srikant P. S., 2004, Journal of Astrophysics and Astronomy, 25, 67
Bull et al. 2015, ApJ, 803, 21
Chatterjee S., Sarkar D., Sarkar A. K., Bharadwaj S. 2017 in preparation
Chang T. C., Pen, U. L., Peterson J. B., McDonald P., 2008, Phys Rev. Lett., 100, 091303
Chen X., 2012, International Journal of Modern Physics Conference Series, 12, 256
Chen X., 2015, IAU General Assembly, 22, 2252187
Datta K. K., Roy Choudhury T., Bharadwaj. S., 2007, MNRAS, 378, 119
Delhaize J., Meyer M. J., Staveley-Smith L., Boyle B. J., 201 3, MNRAS, 433, 1398
Eisenstein, D. J., Hu, W. 1998, ApJ, 496, 605.
Gehlot B. K., Bagla J. S., 2017, JApA, Submitted
Ghosh A., Bharadwaj S., Ali, S. S., Chengalur J. N., 2011a, MNRAS, 411, 2426
Ghosh A., Bharadwaj S., Ali S. S., Chengalur J. N., 2011b, MNRAS, 418, 2584

Guha Sarkar, T., Mitra, S., Majumdar, S. & Choudhury, T. R., 2012, MNRAS, 421, 3570
Khandai, N., et al., 2011, MNRAS, 415, 2580
Lanzetta K. M., Wolfe A. M., Turnshek D. A., 1995, ApJ, 440, 435
Lah P. et al., 2007, MNRAS, 376, 1357
Martin A. M., Papastergis E., Giovanelli R., Haynes M. P., Springob C. M., Stierwalt S., 2010, ApJ, 723, 1359
Marthi, V., R., 2017, JApA, Accepted
Marthi, V., R., & Chengalur, J. 2014, MNRAS, 437 (1), 524
Marthi, V., R., Chatterjee, S.,Chengalur, J. , & Bharadwaj S., 2017 submitted to MNRAS.
Masui, K.W., McDonald, P., Pen, U.L., 2010, PhReD, 81, 103527
Meiring J. D. et al., 2011, ApJ, 732, 35
Newburgh, L. B., et al., 2014, Proc. SPIE Int. Soc. Opt. Eng., 9145, 4V
Noterdaeme, P., Petitjean, P., Carithers, W.C., et al. 2012, AAP, 547, L1
Padmanabhan, H., Roy Choudhury, T., Refregier, A., MNRAS, 447, 3745-3755 (2015)
Péroux C., McMahon R. G., Storrie-Lombardi L. J., Irwin M. J .,2003, MNRAS, 346, 1103
Prasad, P., & Subrahmanya, C. R. 2011, Experimental Astronomy, 31, 1
Prochaska, J. X., Wolfe, A. M. 2009, ApJ, 696, 1543
Rao, S., M., Turnshek D., A., 2000, ApJS, 130, 1
Rao S. M., Turnshek D. A., Nestor D. B. 2006, ApJ, 636, 610.
Rhee J., Zwaan M. A., Briggs F. H., Chengalur J. N., Lah P., Oosterloo T., van der Hulst T., 2013, MNRAS, 435, 2693
Rhee, J., Lah, P., Chengalur, J. N., Briggs, F. N., Colless, N. 2016, MNRAS, 460, 2675. arXiv:1605.02006[astro-ph.GA].
Sarkar, A. K., Bharadwaj, S., & Ali, S. S., 2017, JApA, Accepted
Sarkar, D., Bharadwaj, S., Anathpindika, S. 2016, MNRAS, doi: 10.1093/mnras/stw1111.
Seo, H.-J., Dodelson, S., Marriner, J., et al. 2010, ApJ, 721, 164.
Subrahmanya,C.R., Manoharan, P.K., & Chengalur, J.N. 2017a, JApA, Accepted
Subrahmanya,C.R., Prasad, P., Girish, B.S., Somasekhar, R., Manoharan, P.K., & Mittal, S.G. A., 2017b, JApA, Accepted
Swarup, G., Sarma, N. V. G., Joshi, M. N., Kapahi, V. K., Bagri, D. S., Damle, S. H., Ananthakrishnan, S., Balasubramanian, V., Bhave, S. S., Sinha, R. P., 1971, Nature, Phys. Sci., 230, 185.
Swarup G., Ananthakrishnan S., Kapahi V. K., Rao A. P., Subrahmanya C. R., Kulkarni V. K., 1991 , Curr. Sci., 60, 95
Storrie-Lombardi L. J., McMahon R. G., Irwin M. J., 1996, MN- RAS, 283, L79
Visbal, E., Loeb, A., Wyithe, S., 2009, JCAP, 10, 30
Villaescusa-Navarro, F., Viel, M., Datta, K., K., Choudhury, T., R., 2014, JCAP Phys., 9, 5
Wolfe, A.,M., Lanzetta, K.,M., Foltz, C.,B., Chaffee, F.,H., 1995, Ap.J, 454, 698
Wyithe, J. Stuart B., and Abraham Loeb. MNRAS383.2 2008 606-614.
Wyithe, J.S.B., Loeb,A., Geil, P.M. 2008, MNRAS, 383, 1195.
Zwaan M. A., Meyer M. J., Staveley-Smith L., Webster R. L., 2005, MNRAS, 359, L30